Supplementary information for "Experimental observation of exact quantum critical states"

CONTENTS

I. THEORETICAL DETAILS ON THE MOSAIC LATTICE MODEL

In the main text, we experimentally simulate the mosaic lattice model with and without on-site potential and demonstrate its dynamics associated with the density profile of eigenstates. Here, we provide further details regarding the analytic results of the models.

A. Review of global theory of one-frequency cocycle

We begin by reviewing the global theory characterizing the one-dimensional (1D) quasiperiodic systems and applying it to the model investigated in this work. The global theory analyzes the one-frequency SL(2) cocycle, which describes systems with nearest-neighbor hopping and a single incommensurate factor. A well-known example is the Aubry-André-Harper (AAH) model [S1], or the almost-Mathieu operator in mathematics [S2]. Eigenstates in such quasiperiodic systems can be categorized as extended, localized, and critical, which belong to the absolutely continuous, pure point, and singularly continuous spectra, respectively.

The localization properties of the eigenstates can be fully characterized by examining the Lyapunov exponent (LE), denoted as γ, using Avila's global theory [S2]. Consider a generic 1D quasiperiodic system with one-frequency quasiperiodic modulation, with the Hamiltonian given by

$$H/\hbar = \sum_j J_j \left(\sigma_j^+ \sigma_{j+1}^- + \sigma_j^- \sigma_{j+1}^+\right) + \sum_j V_j(\alpha)\sigma_j^+\sigma_j^-. \tag{S1}$$

The one-frequency quasiperiodic modulation for such Hamiltonian means that the hopping coefficients J_j and on-site potential V_j can be modulated by a single frequency, characterized by an irrational number α. For an eigenstate $|\Psi\rangle$ with the energy E, expanded over the real-space basis as $|\Psi\rangle = \sum_j u_j \sigma_j^+ |0^{\otimes N}\rangle$, the Schrödinger equation $H|\Psi\rangle = E|\Psi\rangle$ leads to:

$$J_{j-1}u_{j-1} + J_j u_{j+1} + V_j u_j = E u_j. \tag{S2}$$

The LE for the eigenenergy E, denoted by $\gamma_0(E)$, is derived by considering:

$$\gamma_\epsilon(E) = \lim_{n\to\infty} \frac{1}{2\pi n} \int \ln \left\| \prod_{j=1}^{n} T_j(\theta + i\epsilon) \right\| d\theta, \tag{S3}$$

where $||A||$ is the norm of the matrix A, ϵ is the imaginary part of the complexified θ and T_j is the transfer matrix at site j satisfying $\begin{pmatrix} u_{j+1},\ u_j \end{pmatrix}^{\mathsf{T}} = T_j \begin{pmatrix} u_j,\ u_{j-1} \end{pmatrix}^{\mathsf{T}}$, with

$$T_j = \begin{pmatrix} \frac{E-V_j}{J_j} & -\frac{J_{j-1}}{J_j} \\ 1 & 0 \end{pmatrix}. \tag{S4}$$

The key result from Avila's global theory is that $\gamma_\epsilon(E)$, as a function of ϵ, is convex, continuous and piecewise linear with a quantized *acceleration* $\omega(E;\epsilon)$:

$$\omega(E;\epsilon) = \lim_{\epsilon\to 0^+} \frac{1}{2\pi\epsilon}[\gamma_\epsilon(E) - \gamma_0(E)] = \mathbb{Z}. \tag{S5}$$

The non-negative LE determines the localization properties of the eigenstates: $\gamma(E) > 0$ implies the state with the energy E belongs to the pure point spectrum and is localized with the localization length $\xi(E) = \gamma^{-1}$. Conversely, $\gamma(E) = 0$ indicates the state is delocalized, possessing an infinite localization length. Delocalized states can be further categorized into extended (absolutely continuous spectrum) and critical states (singularly continuous spectrum) [S3]. Critical states, corresponding to the singularly continuous spectrum, can be realized by imposing one of two fundamental conditions on the delocalized states ($\gamma = 0$): either introducing an unbounded quasiperiodic on-site potential or incorporating incommensurately distributed zeros (IDZs) in the hopping terms [S4]. The latter mechanism is the primary focus of our experiment, as the former is generally unfeasible in physical systems due to the requirement of divergent on-site energies. Both conditions effectively partition the 1D system into multiple subchains, prompting the delocalized orbitals to reorganize within these subchains and thereby giving rise to critical states.

B. Generalized mosaic lattice model in the uniform potential limit

We analytically characterize the model in the main text for the limit of nearest-neighbor coupling (i.e., long-range coupling $J^L_{m,n} = 0$) and uniform potential $V_0 = 0$. The Hamiltonian is

$$H/\hbar = \sum_j J_j \left(\sigma_j^+\sigma_{j+1}^- + \sigma_j^-\sigma_{j+1}^+\right), \tag{S6}$$

with

$$J_j = \begin{cases} \lambda & j = 1 \mod 2, \\ 2J\cos(2\pi\alpha j + \theta) & j = 0 \mod 2. \end{cases} \tag{S7}$$

The coupling coefficients exhibit a mosaic pattern, thus we consider the two-fold transfer matrix

$$\begin{aligned} T_j &= \begin{pmatrix} \frac{E}{2J\cos(2\pi\alpha j+\theta)} & -\frac{\lambda}{2J\cos(2\pi\alpha j+\theta)} \\ 1 & 0 \end{pmatrix} \begin{pmatrix} \frac{E}{\lambda} & -\frac{2J\cos(2\pi\alpha j+\theta)}{\lambda} \\ 1 & 0 \end{pmatrix}, \\ &= \frac{1}{2\cos(2\pi\alpha j+\theta)} \begin{pmatrix} \frac{E^2-4J^2\cos^2(2\pi\alpha j+\theta)}{J\lambda} & -E/J \\ E/J & -\lambda/J \end{pmatrix}, \\ &= \frac{1}{2\cos(2\pi\alpha j+\theta)} \tilde{T}_j. \end{aligned} \tag{S8}$$

By complexifying the phase of the system as $\theta \to \theta + i\epsilon$ and taking the limit $\epsilon \to \infty$, we calculate the LE using Eq. S3. The first term can be obtained using Jenson's formula

$$\int_0^{2\pi} \ln \left| \frac{1}{2\cos(\theta + i\epsilon)} \right| d\theta = -2\pi|\epsilon|. \tag{S9}$$

The second term is

$$\begin{aligned} \tilde{\gamma}_\epsilon(E) &= \lim_{n\to\infty} \frac{1}{2\pi n} \int \ln \left\| \prod_{j=1}^{n} \tilde{T}_j(\theta + i\epsilon) \right\| \mathrm{d}\theta, \\ &= \lim_{n\to\infty} \frac{1}{2\pi n} \int \ln \left\| \prod_{j=1}^{n} (J/\lambda) e^{i4\pi\alpha j} e^{i2\theta} e^{2\epsilon} \right\| d\theta, \\ &= \ln|J/\lambda| + 2|\epsilon|. \end{aligned} \tag{S10}$$

Thus we obtain

$$2\gamma_0 = \max\left\{\ln|J/\lambda|, 0\right\}. \tag{S11}$$

The factor 2 arises from the counting of the two-step transfer matrix. For $|\lambda| < |J|$, the system is in the localized phase with the localization length given by

$$\xi = \frac{1}{\gamma_0} = \frac{2}{\ln|J/\lambda|}. \tag{S12}$$

For $|\lambda| > |J|$, the $\gamma_0 = 0$, and the system exhibits a sequence of site indices $\{j_k\}$ where the coupling coefficients vanish in the thermodynamic limit ($J_{j_k} \to 0$), which are the IDZs of the hopping terms. Thus, the system is in the critical phase [S3, S4].

We further numerically compute the phase diagram of the model by directly diagonalizing the Hamiltonian and calculate the fractal dimension (FD) for the mth eigenstate $|\psi\rangle = \sum_{j=1}^{L} u_{m,j}\sigma_j^+|0^{\otimes N}\rangle$, which is defined as FD $= -\lim_{L\to\infty} \ln(\mathrm{IPR})/\ln(L)$, with the inverse

partition ratio given by IPR $= \sum_j |u_{m,j}|^4$. For localized states, FD approaches 0, while for extended states, FD approaches 1. Critical states exhibit FD values between 0 and 1. Fig. S1 shows FD as a function of energy E and λ/J, with transitions between localized and critical phases observed, consistent with our analytical results. The FD approaches 0 for $|\lambda| < |J|$, indicating localization, and increases towards a critical regime for $|\lambda| > |J|$. In addition, for the finite system we consider here, the FD is not exactly zero but remains close to zero for the localized states. One can observe that the FD is closer to 0 for smaller λ/J within the localized phase, aligning with the analytical result that a smaller λ/J corresponds to a shorter localization length and more localized compared to larger λ/J.

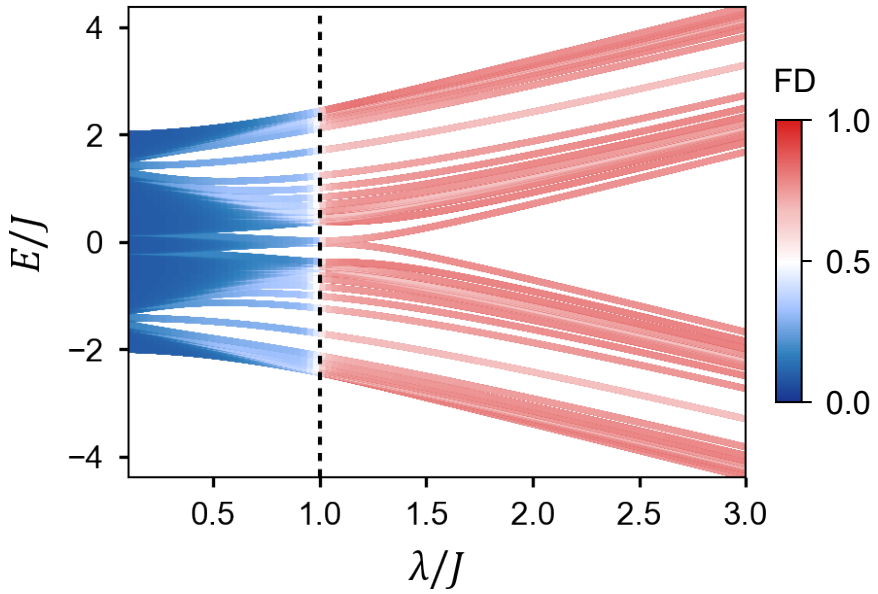

Supplementary Fig. S1. **Phase diagram of generalized mosaic model with $J^L_{m,n} = V_0 = 0$.** Fractal dimension (FD) of the eigenstate as a function of energy E and λ/J for a system size of $L = 2584$. The transition from localized to critical phases occurs as λ/J increases, consistent with the analytic results.

C. Generalized mosaic lattice model along high symmetry lines

We next provide an exact characterization of the model with a mosaic incommensurate on-site potential, while maintaining $J^L_{m,n} = 0$. The Hamiltonian is

$$H/\hbar = \sum_j J_j \left(\sigma_j^+ \sigma_{j+1}^- + \sigma_j^- \sigma_{j+1}^+\right) + \sum_j V_j \sigma_j^+ \sigma_j^-, \tag{S13}$$

where the definition of J_j remains the same as before, and the on-site potential V_j is given by

$$V_j = \begin{cases} 2V_0 \cos[2\pi\alpha(j-1)+\theta] & j = 1 \mod 2, \\ 2V_0 \cos(2\pi\alpha j + \theta) & j = 0 \mod 2. \end{cases} \tag{S14}$$

Introducing the on-site potential generically breaks the solvability of the system; however, it remains analytically tractable along high-symmetry lines where $|V_0| = |J|$. Here we focus on the case $V_0 = J > 0$ without loss of generality. The two-step transfer matrix now becomes

$$\begin{aligned} T_j &= \frac{1}{M} \begin{pmatrix} (E^2 - 2EJM)/J\lambda & -(E/J - M) \\ E/J - M & -\lambda/J \end{pmatrix}, \\ &= \frac{1}{2\cos(2\pi\alpha j + \theta)} \tilde{T}_j, \end{aligned} \tag{S15}$$

with $M = 2\cos(2\pi\alpha j + \theta)$. By complexifying the phase $\theta \to \theta + i\epsilon$ and taking the limit $\epsilon \to \infty$, we calculate the LE as follows:

$$\begin{aligned} 2\gamma_\epsilon &= \frac{1}{2\pi}\int_0^{2\pi} \ln\left|\frac{1}{2\cos(2\pi\alpha j+\theta)}\right| d\theta + \lim_{n\to\infty}\frac{1}{2\pi n}\int \ln\left\|\prod_{j=1}^{n} T_j(\theta + i\epsilon)\right\| d\theta, \\ &= -|\epsilon| + \lim_{n\to\infty}\frac{1}{2\pi n}\int \ln\left\|\prod_{j=1}^{n}\begin{pmatrix} -2E/\lambda & 1 \\ -1 & 0 \end{pmatrix} e^{-i(2\pi a\alpha j+\theta)} e^{\epsilon}\right\| d\theta, \\ &= \ln\left||E/\lambda| + \sqrt{E^2/\lambda^2 - 1}\right|. \end{aligned} \tag{S16}$$

Following the same reasoning as in the previous section, the LE for the system is given by

$$2\gamma_0 = \max\left\{\ln\left||E/\lambda| + \sqrt{E^2/\lambda^2 - 1}\right|, 0\right\}. \tag{S17}$$

The critical energies for the LE transition from zero to a non-zero value, known as the mobility edges (MEs), are

$$E_c = \pm\lambda. \tag{S18}$$

For eigenenergies $|E| > |\lambda|$, the corresponding eigenstates are localized with the localization length given by

$$\xi(E) = \frac{1}{\gamma_0} = \frac{2}{\ln\left||E/\lambda| + \sqrt{E^2/\lambda^2 - 1}\right|}. \tag{S19}$$

While for the eigenenergies $|E| < |\lambda|$, the $\gamma = 0$, and the system exhibits IDZs in the thermodynamic limit. Consequently, the corresponding eigenstates are critical states.

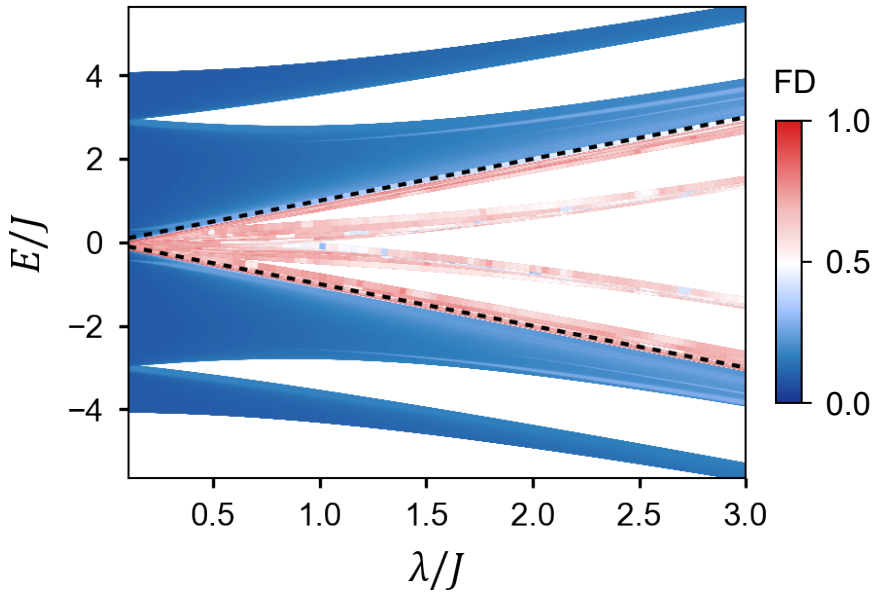

Supplementary Fig. S2. **Phase diagram of generalized mosaic model with $J^L_{m,n} = 0$ and $V_0 = J$.** The fractal dimension (FD) of the eigenstate with the energy E for a system size of $L = 2584$. The dashed lines mark the positions of mobility edges at $E = \pm\lambda$. Eigenstates are localized for energies $|E| > |\lambda|$ and critical for energies $|E| < |\lambda|$, as predicted by the analytical results.

Fig. S2 displays the FD of the eigenstates as a function of energy E for different λ/J. The dashed lines indicate the positions of the MEs at $E = \pm\lambda$. FD approaches 0 for the eigenstates with $|E| > |\lambda|$, confirming their localized nature, and takes values between 0 and 1 for eigenstates with $|E| < |\lambda|$, consistent with critical states. Additionally, for the finite system size considered ($L = 2584$), the FD does not reach exactly zero but remains close to zero in the localized phase. FD is closer to 0 for eigenstates with energies distant from the MEs. This observation aligns with analytical predictions: eigenstates located far from the MEs exhibit shorter localization lengths, resulting in lower FD values. As eigenstates approach the MEs, the localization length increases and diverges at the MEs, leading to higher FD values.

D. Finite size scaling for generalized mosaic lattice model

We investigate the finite size scaling of fractal dimension for the eigenstates in the generalized mosaic lattice model without long-range coupling, i.e., $J^L_{m,n} = 0$, in the presence and

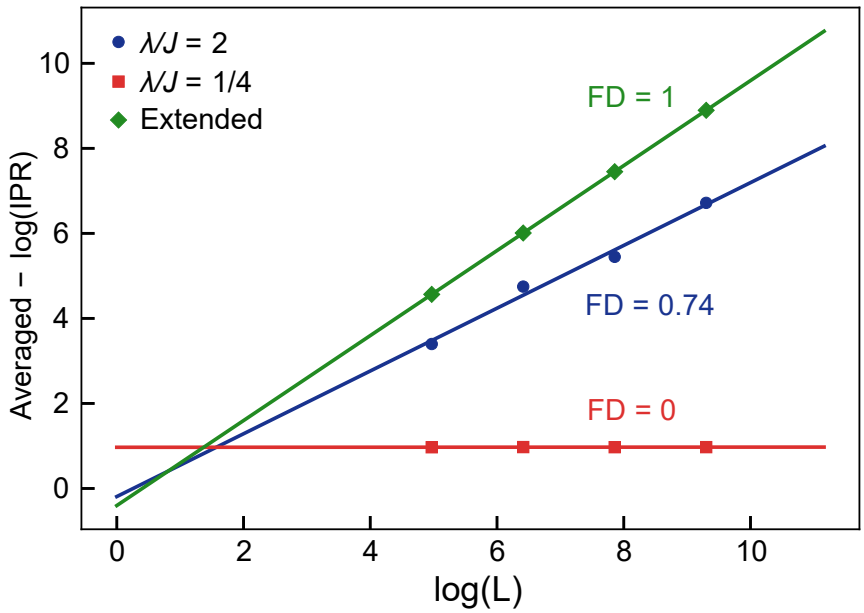

Supplementary Fig. S3. **Finite size scaling analysis of the fractal dimension.** Plot of the averaged $-\log(\text{IPR})$ of all eigenstates versus $\log(L)$ for system size ranging from $L = 144$ to $L = 10946$. Solid lines represent linear fits, with their slopes corresponding to the fractal dimensions. The fitted FD values are zero in the localized phase and approximately 0.74 in the critical phase for this model. And the fitted FD is 1 in the extended phase.

absence of a quasiperiodic on-site potential. We numerically perform the finite size scaling from system sizes $L = 144$ to $L = 10946$ to evaluate the fractal dimension of the model in the thermodynamic limit $L \to \infty$. This involves calculating the inverse partition ratio (IPR) for each finite size system and then analyzing the scaling of IPR as a function of L. The slope of the logarithmic plot, $-\log(\text{IPR})$ versus $\log(L)$, yields the fractal dimension in the thermodynamic limit. Note that in the numerical calculation of this section, we consider the averaged fractal dimension (FD) of all eigenstates in pure phases without mobility edges ($V_0 = 0$). In the presence of mobility edges ($V_0 = J$), it corresponds to the averaged FD of all eigenstates within the localized and critical regimes.

We first present the finite size scaling results in Fig. S3 for the case of $\lambda = J/4$ and $\lambda = 2J$ while keeping $V_0 = 0$, corresponding to the localized phase and critical phase, respectively, which are the parameter regimes of Fig. 3a in the main text. To provide a comprehensive analysis, we also include the finite size scaling results for the extended phase, modeled using a Hamiltonian consisting of uniform nearest-neighbor hopping terms. As the system size

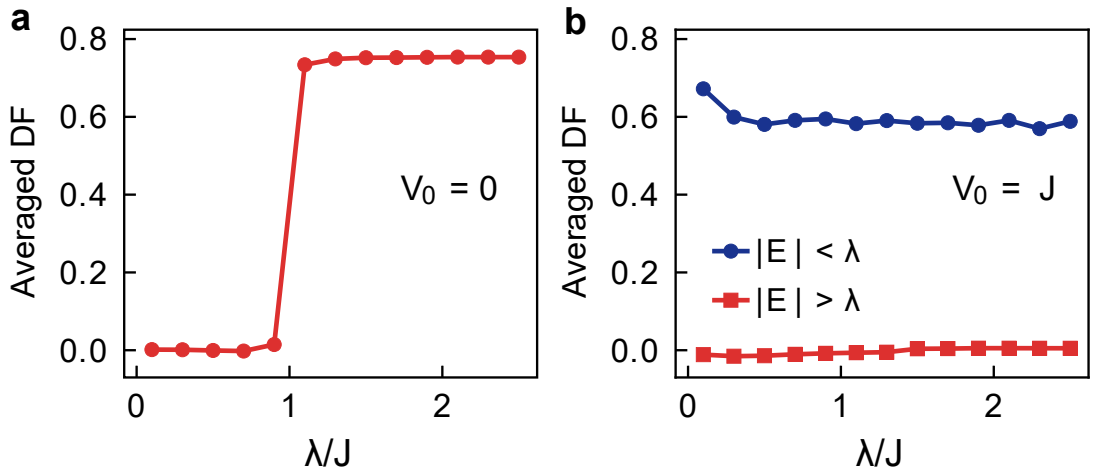

Supplementary Fig. S4. **Fractal dimension at thermodynamic limit for varying λ/J.** The fractal dimension FD of the eigenstates is determined by a linear fit of the averaged $-\log(\text{IPR})$ versus $\log(L)$. **a** For the mosaic model with V_0=0, a phase transition occurs between the localized and critical phases as λ/J varies, with FD shows a transition from zero in the localized phase ($\lambda/J < 1$) to approximately 0.74 in the critical phase ($\lambda/J > 1$). **b** For the mosaic model with $V_0 = J$, the presence of mobility edges $E = \pm\lambda$ separates the localized and critical states. In this case, the FD remains nearly zero in the localized regime, while decreases to a value of approximately 0.6 in the critical regime.

increases towards the thermodynamic limit, the FD for the localized (extended) phase is fitted to approximately 0 (1), respectively. And the FD for the critical phase is fitted to approximately 0.74.

Next, we consider the FD in the thermodynamic limit for the mosaic lattice model under two conditions: without an on-site quasiperiodic potential ($V_0 = 0$) and with a quasiperiodic potential ($V_0 = J$) for different λ/J. For the mosaic lattice model without on-site modulation, the system undergoes a phase transition between a localized phase ($\lambda/J < 1$) and a critical phase ($\lambda/J > 1$). Fig. S4a shows that the averaged FD is nearly zero in the localized phase, while it remains consistently around 0.74 in the critical phase for different values of $\lambda/J > 1$, which shows that the FD remains invariant within the critical phase as λ/J changes. Similarly, for the mosaic model with mobility edges ($V_0 = J$), the FD in the critical regime remains stable across varying λ/J, as shown in Fig. S4b. Here, the FD saturates at a lower value of approximately 0.6 when $\lambda/J > 0.1$, compared to the case

without a quasiperiodic potential shown in Fig. S4a. This reduction of FD can be attributed to the quasiperiodic on-site potential, which limits the spatial extent of the critical states, leading to more localized peaks in each subregion of the wave functions while preserving their multifractal structure and preventing a transition to a fully localized state.

II. CHARACTERIZATION OF INCOMMENSURATELY DISTRIBUTED ZEORS WITH LONG-RANGE COUPLING

In the main text, we demonstrate experimentally that critical states persist under weak long-range coupling and undergo a transition to extended states only when the coupling strength exceeds a threshold magnitude, which removes all the IDZs. To further elucidate this phenomenon, we first model large systems using next-nearest neighbor (NNN) hopping terms as a minimal representation of long-range interactions. Numerical simulations confirm that critical states remain robust until the NNN hopping amplitude reaches a threshold value.

We further use renormalization group (RG) analysis to systematically characterize the transition from critical states to extended states in the presence of long-range coupling. We first show the robustness of the critical states protected by the IDZz, by showing a finite transition NNN hopping coupling strength. This indicates that critical states will be driven into extended states only when the NNN coupling exceeds a finite threshold. To explain the smaller transition long-range coupling observed in the main text, we further introduce the next-next-nearest neighbor (NNNN) coupling. The RG calculation shows that, in the presence of the NNNN coupling, the transition threshold of NNN coupling is reduced. This explains the smaller transition long-range coupling in the main text since the 2D geometry of our system involves various ranges of long-range coupling.

A. Numerical demonstration

To show how the IDZs preserve in the presence of long-range coupling, and as a result, give rise to critical states. Here we consider the 1D mosaic lattice model, with the minimal long-range coupling modeled by the next-nearest neighbor (NNN) coupling J_{nn}, the Hamiltonian

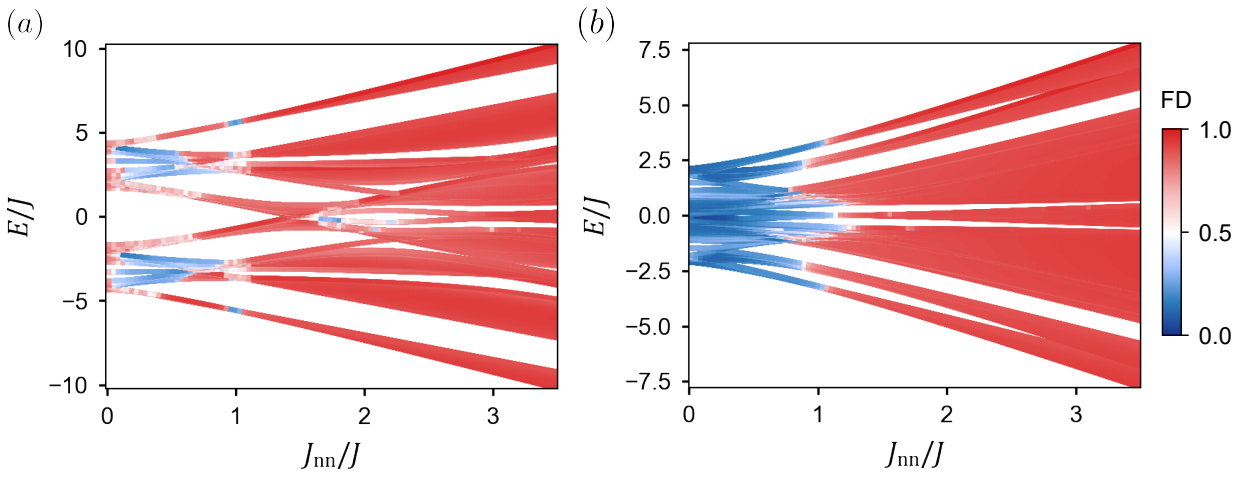

Supplementary Fig. S5. **Mosaic model with long-range coupling. a** Fractal dimension as a function of energy E/J and the next nearest coupling $J_{\rm nn}/J$. Here $\lambda/J = 3$ and system is in critical phase when $J_{\rm nn} = 0$. For such finite but large system size, the critical state will be driven to extended state when $J_{\rm nn}/J$ is large enough. **b** Fractal dimension as a function of energy E/J and the next nearest coupling $J_{\rm nn}/J$. $\lambda/J = 0.5$ and the system is in localized phase when $J_{\rm nn} = 0$. Similarly, system persists in localized phase until $J_{\rm nn}$ is larger than a threshold. For both cases, the system sizes are $L = 2584$.

is then given by

$$H = \sum_j J_j(\sigma_j^\dagger \sigma_{j+1}^- + \sigma_{j+1}^\dagger \sigma_j^-) + \sum_j J_{\rm nn}(\sigma_j^\dagger \sigma_{j+2}^- + \sigma_{j+2}^\dagger \sigma_j^-), \tag{S20}$$

with the J_i in a mosaic manner, namely $J_j = \lambda$ for j is odd and $J_j = 2J\cos(2\pi\alpha j + \theta)$ for j is even.

We first start from the critical phase, namely we introduce NNN coupling on top of the critical state by considering the case $\lambda = 3J$. As expected, when $J_{\rm nn}/J$ is not so large, the system still contains critical states, as indicated in Fig. S5(a). And for sufficiently large $J_{\rm nn}/J$, then the system enters the extended phase.

We then start from the localized phase with $\lambda = 0.5J$, then turning on $J_{\rm nn}$ neither drives the localized state into extended state immediately, only when it exceeds a threshold as shown in Fig. S5(b). Moreover, in this case, there are no critical states in the whole spectrum. This also manifests the mechanism that the critical states are generated by the IDZs on top of the delocalized states.

B. Renormalization group for the long-range mosaic model

1. *Review of the renormalization group approach*

We first briefly review the procedure of the renormalization group approach. We consider a generic 1D Hamiltonian $H/\hbar = \sum_j t_j(\sigma_j^+\sigma_{j+1}^- + \sigma_j^-\sigma_{j+1}^+) + V_j\sigma_j^+\sigma_j^-$ with quasiperiodic modulation $\cos(2\pi\alpha j + \theta)$, here the irrational number α is an irrational number that can be approached by Diophantine approximation, for example, the golden ratio number that can be approached by the Fibonacci series $\alpha = F_{n-1}/F_n$, with F_n being the Fibonacci series.

This approach aims at determining which localization phases the given state flows to by calculating the relevant parameter of the associated dispersion. Specifically, we first approximate the incommensurate parameter in the quasiperiodic modulation by a commensurate integer $\alpha = \lim_{n\to\infty} F_{n-1}/F_n$, with F_n being the Fibonacci number is the system size L. The original Hamiltonian then becomes periodic and exhibits band structure. Then we introduce the quasi-momentum κ_x along x-direction by the twisted boundary condition or equivalently threading a flux. And we map the phase offset θ as the quasi-momentum in y-direction as κ_y. Then one can obtain the corresponding Bloch Hamiltonian $\mathcal{H}^{(n)}(\kappa_x, \kappa_y)$. Then we identify which dispersion within the Bloch Hamiltonian becomes relevant and irrelevant as we iterate the size of the unit cell. Specifically, we shall investigate the characteristic polynomial given by $P^{(n)} = \det[H^{(n)}(\kappa_x, \kappa_y) - E]$ for the state with the energy E, which can be rewritten the $P^{(n)}$ as the form

$$\begin{aligned} P^{(n)}(E;\kappa_x,\kappa_y) = {} & t_R^{(n)}(E)\cos(\kappa_x + \kappa_x^0) + V_R^{(n)}(E)\cos(\kappa_y + \kappa_y^0) \\ & + C_R^{(n)}(E)\cos(\kappa_x + \tilde{\kappa}_x^0)\cos(\kappa_y + \tilde{\kappa}_y^0) \\ & + \epsilon_R^{(n)}(E,\varphi,\kappa) + T_R^{(n)}(E), \end{aligned} \tag{S21}$$

where $\epsilon_R^{(n)}$ represents higher harmonic terms. The different phases are characterized by investigating how the parameters evolve as $n \to \infty$ by comparing the coefficients of the corresponding dispersions. For the extended phase, the on-site potential becomes irrelevant $\left|C_R^{(n)}/t_R^{(n)}\right|, \left|V_R^{(n)}/t_R^{(n)}\right| \to 0$, for the localized phase, we have an irrelevant hopping $\left|C_R^{(n)}/V_R^{(n)}\right|, \left|t_R^{(n)}/V_R^{(n)}\right| \to 0$ and for the critical phase, both hopping and on-site potential are relevant $\left|C_R^{(n)}/V_R^{(n)}\right|, \left|C_R^{(n)}/t_R^{(n)}\right| \geq 1$.

L	$t_{1R}^{(L)}(0)$	$V_{1R}^{(L)}(0)$	$t_{2R}^{(L)}(0)$	$V_{2R}^{(L)}(0)$	$C_R^{(L)}(0)$
3	0	0	$2J_{\rm nn}^6$	$-2J^6$	$4J^3\lambda\left(3J_{\rm nn}^2+\lambda^2\right)$
5	0	0	$2J_{\rm nn}^{10}$	$-2J^{10}$	$4J^5\lambda\left(5J_{\rm nn}^4+5J_{\rm nn}^2\lambda^2+\lambda^4\right)$
7	0	0	$2J_{\rm nn}^{14}$	$-2J^{14}$	$4J^7\lambda\left(7J_{\rm nn}^6+14J_{\rm nn}^4\lambda^2+7J_{\rm nn}^2\lambda^4+\lambda^6\right)$

Supplementary Table I. Numerical results for the coefficients of the first three unit cells $L=3$, $L=5$ and $L=7$.

2. Renormalization group analysis for the next-nearest neighbor coupling

To show how the IDZs preserve in the presence of long-range coupling, and as a result, give rise to critical states. Here we consider the 1D mosaic lattice model, with the minimal long-range coupling modeled by the next-nearest (NN) neighbor coupling $J_{\rm nn}$, the Hamiltonian is then given by

$$H/\hbar=\sum_j J_j(\sigma_j^+\sigma_{j+1}^-+\sigma_j^-\sigma_{j+1}^+)+\sum_j J_{\rm nn}(\sigma_j^+\sigma_{j+2}^-+\sigma_j^-\sigma_{j+2}^+), \tag{S22}$$

with the J_j in a mosaic manner, namely $J_j=\lambda$ for j is odd and $J_j=2J\cos(2\pi\alpha j+\theta)$ for j is even. To facilitate the discussion, we first consider the transition from critical to extended state of zero energy state, and then generalize it to the finite energy. For $E=0$, the characteristic polynomial is given by

$$\begin{aligned}P^{(L)}(0;\varphi,\kappa)=&\,t_{1R}^{(L)}\cos(\kappa_x+\kappa_x^0)+V_{1R}^{(L)}\cos(\kappa_y+\kappa_y^0)\\&+t_{2R}^{(L)}\cos[2(\kappa_x+\kappa_x^0)]+V_{2R}^{(L)}\cos[2(\kappa_y+\kappa_y^0)]\\&+C_R^{(L)}\cos(\kappa_x+\tilde{\kappa}_x^0)\cos(\kappa_y+\tilde{\kappa}_y^0)+\epsilon_R^{(n)}(E=0,\varphi,\kappa)+T_R^{(n)}(E=0).\end{aligned} \tag{S23}$$

Here L is the size of the commensurately approximated unit cell $L=F_n$. The characteristic polynomial for any generic approximated unit cell L for the energy E is given by

$$P^{(L)}(E;\varphi,\kappa)=\det\begin{pmatrix}M_0(E) & \Pi_x^\dagger & 0 & \dots & \Pi_x\\ \Pi_x & M_1(E) & \ddots & \ddots & \vdots\\ 0 & \ddots & \ddots & \ddots & 0\\ \vdots & \ddots & \ddots & \ddots & \Pi_x^\dagger\\ \Pi_x^\dagger & \dots & 0 & \Pi_x & M_{L-1}(E)\end{pmatrix}, \tag{S24}$$

with the $M_j(E)$ and Π_x being two-by-two matrices, which are given by

$$M_j(E) = \begin{pmatrix} 2J\cos[2\pi(j-1)\alpha + k_y] - E & 0 \\ 0 & -2J\cos[2\pi(j-1)\alpha + k_y] - E \end{pmatrix}. \tag{S25}$$

and

$$\Pi_x = \begin{pmatrix} e^{-ik_x}(J_{\rm nn} - \frac{\lambda}{2}) & \frac{1}{2}e^{-ik_x}\lambda \\ -\frac{1}{2}e^{-ik_x}\lambda & e^{-ik_x}(J_{\rm nn} + \frac{\lambda}{2}) \end{pmatrix} \tag{S26}$$

Notice that under the transformation $E \to -E$, $k_x \to k_x + \pi$ and $k_y \to k_y + \pi$, the determinant remains the same. Since L is odd, under this transformation, we have $\kappa_x = Lk_x \to \kappa_x + L\pi$ and $\kappa_y = Lk_y \to \kappa_y + L\pi$ altered by an odd number of π. Therefore, we have

$$\begin{aligned} t_{1R}^{(L)}(-E) &= -t_{1R}^{(L)}(E), \\ V_{1R}^{(L)}(-E) &= -V_{1R}^{(L)}(E), \\ t_{2R}^{(L)}(-E) &= t_{2R}^{(L)}(E), \\ V_{2R}^{(L)}(-E) &= V_{2R}^{(L)}(E), \\ C_{R}^{(L)}(-E) &= C_{R}^{(L)}(E). \end{aligned} \tag{S27}$$

Therefore for the zero eigenenergy $E = 0$, we have

$$t_{1R}^{(L)}(0) = 0, \quad V_{1R}^{(L)}(0) = 0. \tag{S28}$$

From the renormalized on-site coupling, we can see that to accumulate a k_y-dependence of e^{i2Lk_y}, the only choice is to multiply $2L$ diagonal terms together, therefore we have the normalized on-site potential strength

$$V_{2R}^{(L)}(0) = -2J^{2L}. \tag{S29}$$

Similarly, for the renormalized hopping coupling, to accumulate a k_x-dependence of e^{i2Lk_x}, one must multiply $2L$ terms with e^{ik} together. By choosing any $-e^{ik}\lambda$ term, the possibility of choosing two $e^{ik}J_{\rm nn}$ terms is eliminated, then one cannot find $2L$ terms with e^{ik} to be multiplied. Therefore the only choice is to multiply $2L$ $e^{ik}J_{\rm nn}$ terms together, which gives normalized hopping coefficient as

$$t_{2R}^{(L)}(0) = 2J_{\rm nn}^{2L}. \tag{S30}$$

The renormalized hopping coupling for the critical states $C_R^{(L)}(0)$ can be understood via incoherent superposition between different contributions. To obtain such k_X and k_y dependence, one will have L terms with e^{ik_X} and L terms with e^{ik_y} multiplied together. Thus one must multiply L factors of $\pm\frac{J}{2}e^{i(k_y+2p\pi\alpha)}$ terms and a total of L factors of $e^{ik_x}J_{\rm nn}$ or L factors of $-e^{ik_x}\lambda$ terms together. Therefore each contribution to the total factor has a random phase factor due to the incommensurate α, resulting in an incoherent superposition with the combinatorial multiplicity to $\mathcal{O}(1)$ under exponential order at $L\to\infty$. Then since the infinite summation of a geometric progression is of order $\mathcal{O}(1)$, the value at $L\to\infty$ is determined by taking as much only $e^{ik}J_{\rm nn}$ or only $-e^{ik}\lambda$ terms as possible. Therefore, we obtain the renormalized hopping coupling for the critical states as

$$C_R^{(L)}(0)\sim J^L\left(J_{\rm nn}^L+\lambda^L\right). \tag{S31}$$

The condition for the emergence of extended state in the presence of next-nearest coupling can be identified by $V_{2R}^{(L)}(0)/t_{2R}^{(L)}(0)\to 0$ and $C(0)/t_{2R}^{(L)}(0)\to 0$, therefore the critical state at $E=0$ will be driven into the extended state if

$$J_{\rm nn}>\max\left(J,\sqrt{J\lambda}\right), \tag{S32}$$

which indicates that only if the next-nearest coupling is larger than a certain threshold, the critical states will be driven into the extended states.

3. *Inclusion of next-next-nearest neighbor coupling*

In this subsubsection, we further show that introducing the next-next-nearest neighbor coupling will decrease the transition threshold for $J_{\rm nn}$ obtained in Eq. (S32). For simplicity of the RG calculation, we introduce the next-next-nearest neighbor coupling on the even site, whose Hamiltonian is given by

$$H=-\mu\sum_{j=\text{even}}(\sigma_{j+3}^{+}\sigma_j^{-}+\sigma_j^{+}\sigma_{j+3}^{-}). \tag{S33}$$

If we relabel the odd/even site as the A/B sublattice, then the eigenvalue equation $H|\psi\rangle=E|\psi\rangle$, with $|\psi\rangle=\sum_{j,s=\{A,B\}}u_{j,s}$ takes the form

$$\begin{pmatrix}J_{\rm nn} & -\lambda\\ -\mu & J_{\rm nn}\end{pmatrix}u_{j-1}+\begin{pmatrix}J_{\rm nn} & -\mu\\ -\lambda & J_{\rm nn}\end{pmatrix}u_{j+1}+\begin{pmatrix}0 & 2J\cos(2\pi\alpha j)\\ 2J\cos(2\pi\alpha j) & 0\end{pmatrix}u_j=Eu_j, \tag{S34}$$

with a unitary transformation, the eigenvalue equation becomes

$$\begin{pmatrix} J_{\rm nn}-t_+ & -t_- \\ t_- & J_{\rm nn}+t_+ \end{pmatrix} u_{j-1} + \begin{pmatrix} J_{\rm nn}-t_+ & t_- \\ -t_- & J_{\rm nn}+t_+ \end{pmatrix} u_{j+1} + \\ + \begin{pmatrix} 2J\cos(2\pi\alpha j) & 0 \\ 0 & -2J\cos(2\pi\alpha j) \end{pmatrix} u_j = E u_j, \tag{S35}$$

with $t_\pm = (\lambda \pm \mu)/2$. Then the characteristic polynomial takes the same form as Eq. (S24), with the same $M_j(E)$ as the case $\mu = 0$, and the modified Π_x as

$$\Pi_x = \begin{pmatrix} e^{-ik_x\left(J_{\rm nn}-\frac{\lambda+\mu}{2}\right)} & e^{-ik_x\frac{\lambda-\mu}{2}} \\ -e^{-ik_x\frac{\lambda-\mu}{2}} & e^{-ik_x\left(J_{\rm nn}+\frac{\lambda+\mu}{2}\right)} \end{pmatrix}. \tag{S36}$$

Following the same logic, for the zero eigenenergy $E = 0$, we have

$$t_{1R}^{(L)}(0) = 0, \quad V_{1R}^{(L)}(0) = 0, \quad V_{2R}^{(L)}(0) = -2J^{2L}. \tag{S37}$$

The renormalized hopping coupling is contributed from the product of either $J_{\rm nn} \times J_{\rm nn}$ or the term $(-\lambda)(-\mu)$, which gives

$$t_{2R}^{(L)}(0) = 2\sum_{l=0}^{L} C_L^l J_{\rm nn}^2(-\lambda)(-\mu) = 2\sqrt{J_{\rm nn}^2+\lambda\mu}^{2L} \tag{S38}$$

The renormalized hopping coupling for the critical states C_R^L can be obtained from the same logic in the last subsubsection, which is given by

$$C_R^{(L)}(0) \sim J^L\left(J_{\rm nn}^L + \lambda^L + \mu^L\right). \tag{S39}$$

From the results Eq. (S37), Eq. (S38) and Eq. (S39), we can see the next-next-nearest neighbor coupling further decreases the transition threshold of $J_{\rm nn}$ for extended states. In particular, when μ is small, i.e. $\mu < \lambda$, one finds that $C_R^{(1)}(0)$ under large L limit is independent of μ, yet $t_{2R}^{(2)}(0)$ increases with μ, thus one requires a smaller $J_{\rm nn}$ to drive critical states into extended states. More precisely, the condition for the emergence of extended state is

$$\frac{V_{t_{2R}}^{(L)}(0)}{t_{2R}^{(L)}(0)} \to 0, \quad \frac{C_{t_{2R}}^{(L)}(0)}{t_{2R}^{(L)}(0)} \to 0 \tag{S40}$$

which is to solve the condition

$$\frac{J^{2L}}{\sqrt{J_{\rm nn}^2+\lambda\mu}^{2L}} \to 0, \quad \frac{J^L(J_{\rm nn}^L+\lambda^L+\mu^L)}{2\sqrt{J_{\rm nn}^2+\lambda\mu}^{2L}} \to 0 \tag{S41}$$

at $L \to \infty$, this gives

$$J_{\rm nn} \in \left(\sqrt{J\max\left(J,\lambda,\mu\right)-\lambda\mu},\max(\lambda,\mu)\right)\bigcup\left(\max\left[\sqrt{J^2-\lambda\mu},\lambda,\mu\right],\infty\right), \tag{S42}$$

which can be unified as

$$J_{\rm nn} > \sqrt{J\max\left(J,\lambda,\mu\right)-\lambda\mu}. \tag{S43}$$

This shows that introducing the next-next-nearest neighbor coupling μ will modify the transition condition [Eq. (S32)] at $\mu = 0$, indicating the long-range coupling further decreases the transition threshold of $J_{\rm nn}$.

III. ADDITIONAL INFORMATION FOR THE DYNAMICAL CHARACTERIZATION

This section provides supplementary details regarding the time evolution presented in the main text. We first review the properties of several key quantities used to characterize the dynamics of critical states, and then introduce specific generalizations tailored to our experimental systems.

In the main text, we analyze the time evolution of the fractal dimension, or equivalently, the dynamical fractal dimension $\mathcal{D}(t)$. To distinguish it from the fractal dimension (FD) obtained from the eigenstates of the Hamiltonian, the dynamical fractal dimension is defined as:

$$\mathcal{D}(t) = -\frac{\log\sum_j |u_{m,j}(t)|^4}{\log N}, \tag{S44}$$

where the $u_{m,j}(t)$ are the time dependent coefficients of the state in the real-space basis, which is given by $|\psi(t)\rangle = \sum_{j=1}^{N} u_{m,j}\sigma_j^+|{\rm vac}\rangle$. The dynamical fractal dimension is closely related to the second-order participation entropy S_2 [S5], up to a constant, where:

$$S_2 = -\log\sum_{j=1}^{N}|u_{m,j}(t)|^4. \tag{S45}$$

Both the dynamical fractal dimension $\mathcal{D}(t)$ and dynamical participation entropy $S_2(t)$ quantify the extent to which a quantum state spans the real space. These definitions can be generalized to many-body systems to measure the spread of quantum states in the Hilbert space [S6].

To probe the phase diagram of the system described in the main text, we utilize the time-averaged dynamical fractal dimension, defined as:

$$\overline{\mathcal{D}} = \frac{1}{t_f}\int_0^{t_f}[\mathcal{D}(\tau) - \mathcal{D}(0)]d\tau, \tag{S46}$$

which smooths out oscillations over time and serves as a reliable indicator of the phase of the system.

A. Wave packet dynamics

Wave packet dynamics is a widely used method for characterizing the dynamical behavior of quantum states. The localized, extended, and critical phases can be distinguished by monitoring the time evolution of an initial wave packet, typically initialized as a Gaussian distribution with half-width a, centered at the site j_0:

$$\psi_j(t=0) = \frac{1}{\sqrt{\sqrt{\pi}a}}e^{-(j-j_0)^2/2a^2}, \tag{S47}$$

The evolution can be characterized by the mean square displacement $W(t)$, which measures the width of the wave packet and is defined as:

$$W(t) = \left[\sum_j (j-j_0)^2 |\langle\psi(t)|j\rangle|^2\right]^{1/2}. \tag{S48}$$

In the long time limit, $W(t)$ exhibits universal scaling:

$$W(t) \sim t^{\kappa}, \tag{S49}$$

where the dynamical exponent κ takes characteristic values depending on the phase: $\kappa = 1$ for extended phase, $k = 0$ for localized phase, and $0 < \kappa < 1$ for critical phase [S7–S9].

In our experimental implementation, we replace the initial Gaussian wave packet with a single-site occupation. To improve robustness against local noise in experiments, we redefine the mean square width using:

$$W(\tau) = \sum_j \sqrt{|j-j_0|}|\langle\psi(\tau)|j\rangle|^2. \tag{S50}$$

Instead of focusing on the long-time universal behavior of $W(\tau)$, we analyze its early-time dynamics as a complementary marker for the dynamical fractal dimension. Specifically, we

calculate the integrated width:

$$M(t_f) = \frac{1}{t_f} \int_0^{t_f} [W(\tau) - W(0)] d\tau, \tag{S51}$$

which captures the early-time spin dynamics in the system.

IV. DEVICE FABRICATION AND ASSEMBLY

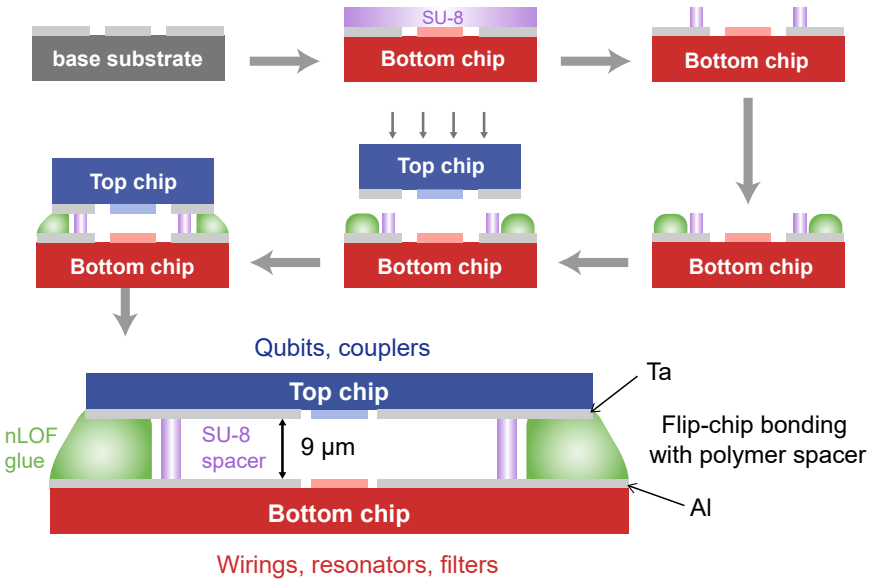

Supplementary Fig. S6. **Fabrication process of the quantum processor.** The processor consists of a top qubit chip and a bottom carrier chip, bonded face-to-face using SU-8 and nLOF glue.

The experiment in this work is carried out on a two-dimensional (2D) superconducting quantum processor consisting of 66 frequency-tunable transmon qubits and 110 tunable couplers. The processor comprises a top chip and a bottom carrier chip, bonded face-to-face using SU-8 and nLOF glue [S10]. The top chip hosts the qubits and couplers, whereas the bottom carrier chip hosts the readout resonators as well as control and readout wiring circuitries. The fabrication and assembly process of the quantum processor, as illustrated in Fig. S6, involves the following steps:

1. A 100 nm aluminum is deposited onto a sapphire wafer using electron beam evaporation for the bottom chip; and a 100 nm tantalum film is deposited onto another sapphire wafer using sputtering for the top chip respectively.

2. Large-scale structures, including the control and readout circuits on the bottom chip, as well as the capacitor pads for the qubits and couplers on the top chip, are realized through optical lithography and subsequent wet etching.

3. To mitigate signal crosstalk, SiO_2-supported bridges are created on the bottom chip to shield critical circuits.

4. The Al-AlO_x-Al Josephson junctions are patterned on the top chip via electron beam lithography and fabricated using the double-angle electron beam evaporation.

5. Bandage technology [S11] is employed to establish a galvanic connection between the aluminum junctions deposited in step 4 and the tantalum film deposited in step 1.

6. 9-μm-tall SU-8 photoresist is positioned at the corners of the bottom carrier chip as a spacer between the top and bottom chips, and then the top and bottom chips are bonded together using nLOF glue.

The device fabricated using the above technique is robust in performance after several cycles of cooling down and warming up, and the bonding process of two separate chips through polymer spacers enables us to recycle the bottom (top) chip if the performance of the other chip is not good after cooling down and being measured, which increases the productivity of our fabrication.

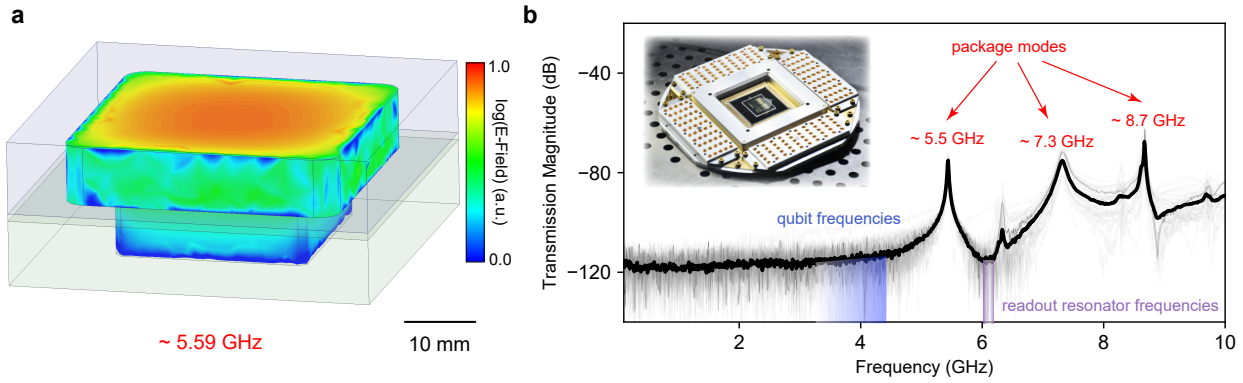

Supplementary Fig. S7. **Package modes. a** Example EM simulation of the box model revealing the package mode at 5.59 GHz (others larger than 7.0 GHz). The box modes in real device can slightly vary as the bonding connections are involved. **b** The transmission magnitudes for the device package are measured by vector network analyzer via multiple ports (grey lines) and being averaged (black line). The probed package modes are marked by the red arrows, which are detuned from the working frequencies of qubits and readout resonator. The inset (upper left) shows an example photograph of the package with the cover removed.

Care must be taken when designing the package for quantum chips of this scale [S12, S13]. Fig. S7 shows the electromagnetic (EM) simulation and measurement of the package mode for our device. EM simulation of the package, as shown in Fig. S7a, reveals the lowest package mode at 5.59 GHz. In Fig. S7b, we measure the transmission magnitudes for the device package by vector network analyzer via multiple ports. The lowest package mode is probed at 5.5 GHz, which is close to the simulated value. The slight deviation could be due to the bonding connections involved in the real device. The working frequencies of the qubits ($\sim$ 4.2 GHz) are well below the fundamental box mode. The readout resonators ($\sim$ 6.2 GHz) are strategically positioned between the fundamental box mode at 5.5 GHz and the secondary mode at 7.3 GHz.

V. EXPERIMENTAL SETUP

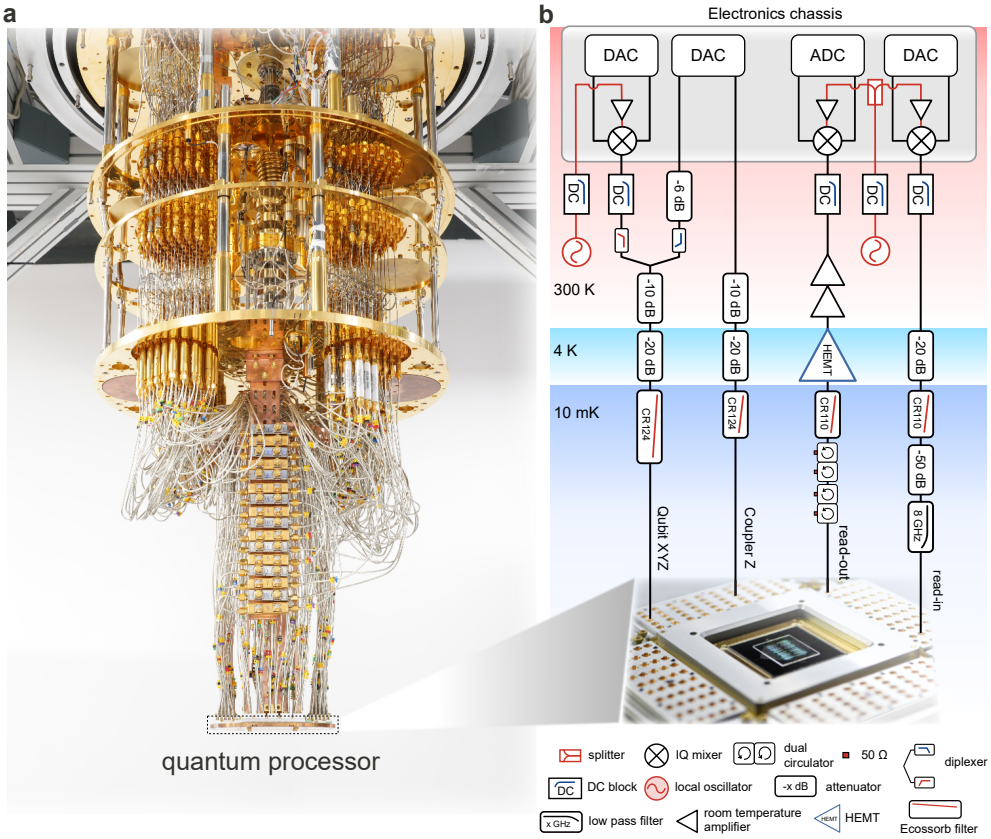

Supplementary Fig. S8. **Experimental setup.** **a** Photograph of the cryogenic setup with the mounted quantum processor. **b** Illustration for room-temperature and cryogenic wiring.

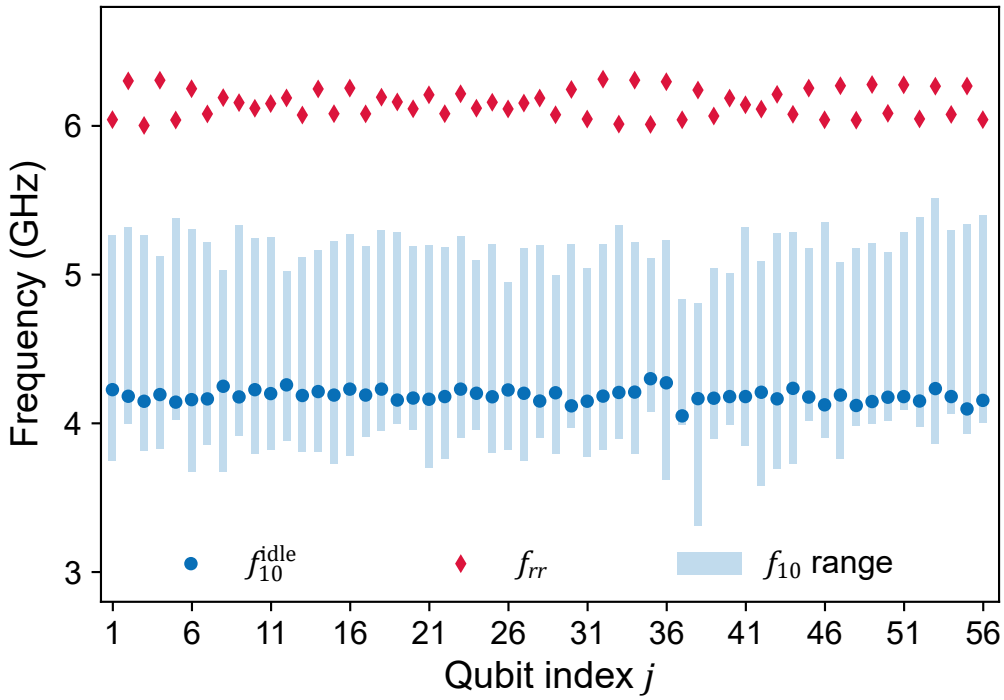

Supplementary Fig. S9. **Characterization of qubit frequencies f_{10} and readout resonator frequencies f_{rr}.** The blue lines denote the tuning range of qubit frequencies, the blue dots denote the qubit idling frequencies, and the red lines with dots denote the readout resonator frequencies.

The quantum processor is mounted on the mixing chamber plate of a dilution refrigerator (DR) with a temperature of around 10 mK, as shown in Fig. S8a. The room-temperature and cryogenic wirings in our experimental setup are illustrated in Fig. S8b, in which we use custom-made digital-to-analog converter (DAC) and analog-to-digital converter (ADC) circuit boards for qubit control and measurement, respectively. In the quantum processor, the 66 qubits are arranged in a square lattice, from which we select 56 qubits arranged in a 1D array, as shown in Fig. S11a. Each nearest-neighbor (NN) qubit pair is connected by a tunable coupler to control the effective coupling strength between qubits. The qubits have two asymmetric Josephson junctions with $E_{J1}/E_{J2} = 3.6$, where E_{J1} and E_{J2} are the Josephson energies of the two junctions. The frequency of each qubit can be individually adjusted by varying the corresponding external flux through the Z control line and ranges from approximately 3.9 GHz to 5.2 GHz, as shown in Fig. S9 and Fig. S11b. Typical qubit relaxation time T_1 at their idle frequencies are shown in Fig. S11c. The state of the qubit can be deduced by measuring the state-dependent transmission of the readout resonator

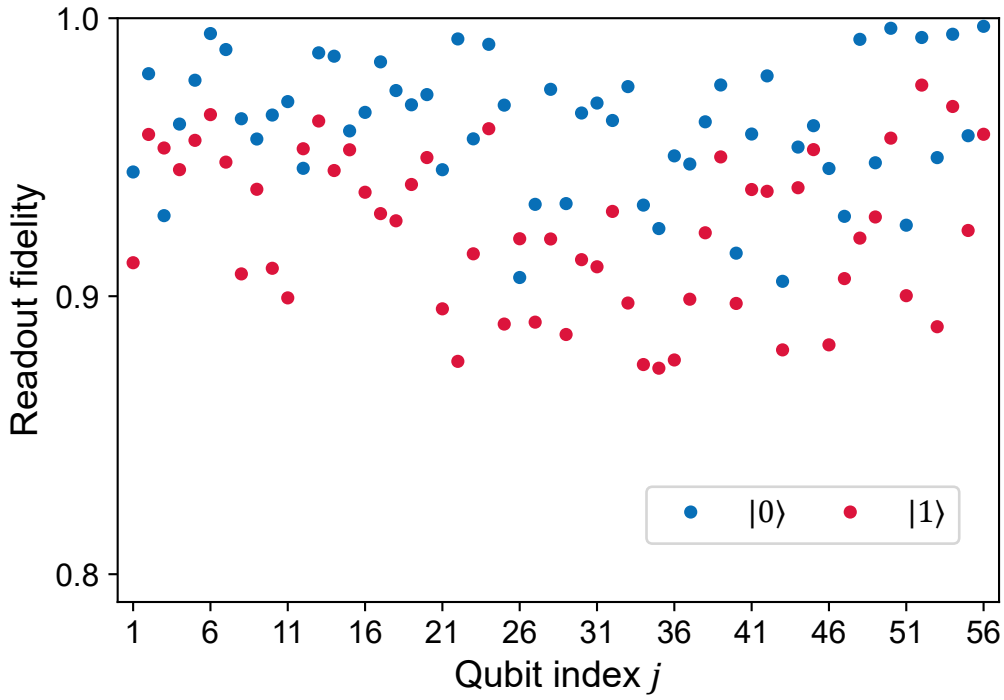

Supplementary Fig. S10. **Characterization of readout fidelities for states** $|0\rangle, |1\rangle$**.** The blue dots denote the readout fidelities of $|0\rangle$, and the red dots denote the readout fidelities of $|1\rangle$.

using the dispersive readout scheme, where the dedicated readout resonator with frequency around 6.15 GHz is coupled to each qubit. Fig. S10 and Fig. S11d display the qubit readout fidelities, with median values of 0.96 for the $|0\rangle$ state, 0.93 for the $|1\rangle$ state, respectively.

The two floating tunable transmon qubits in our device are capacitively coupled to a floating tunable coupler [S14], and each floating qubit is surrounded by four couplers [S15]. The circuit schematic of the qubit-coupler-qubit system is shown in Fig. S12a, where the effective coupling strength between qubits Q_A and Q_B can be controlled by applying external flux on the corresponding coupler C [S16, S17]. The system of qubits $Q_{A,B}$ and coupler C can be described by the Hamiltonian

$$\begin{aligned} H/\hbar = &\sum_{i=A,B,C} \left(\omega_i a_i^\dagger a_i + \frac{U_i}{2} a_i^\dagger a_i^\dagger a_i a_i\right) + g_{AC}\left(a_A^\dagger a_C + a_A a_C^\dagger\right) + g_{BC}\left(a_B^\dagger a_C + a_B a_C^\dagger\right) \\ &+ g_{AB}\left(a_A^\dagger a_B + a_A a_B^\dagger\right), \end{aligned} \tag{S52}$$

where a_i ($a_i^\dagger$) is the annihilation (creation) operator, ω_i is the qubit or coupler frequencies, U_i is the qubit or coupler anharmonicities, g_{AC} (g_{BC}) is the coupling strength between Q_A (Q_B) and coupler C, and g_{AB} is the coupling strength between Q_A and Q_B. When the

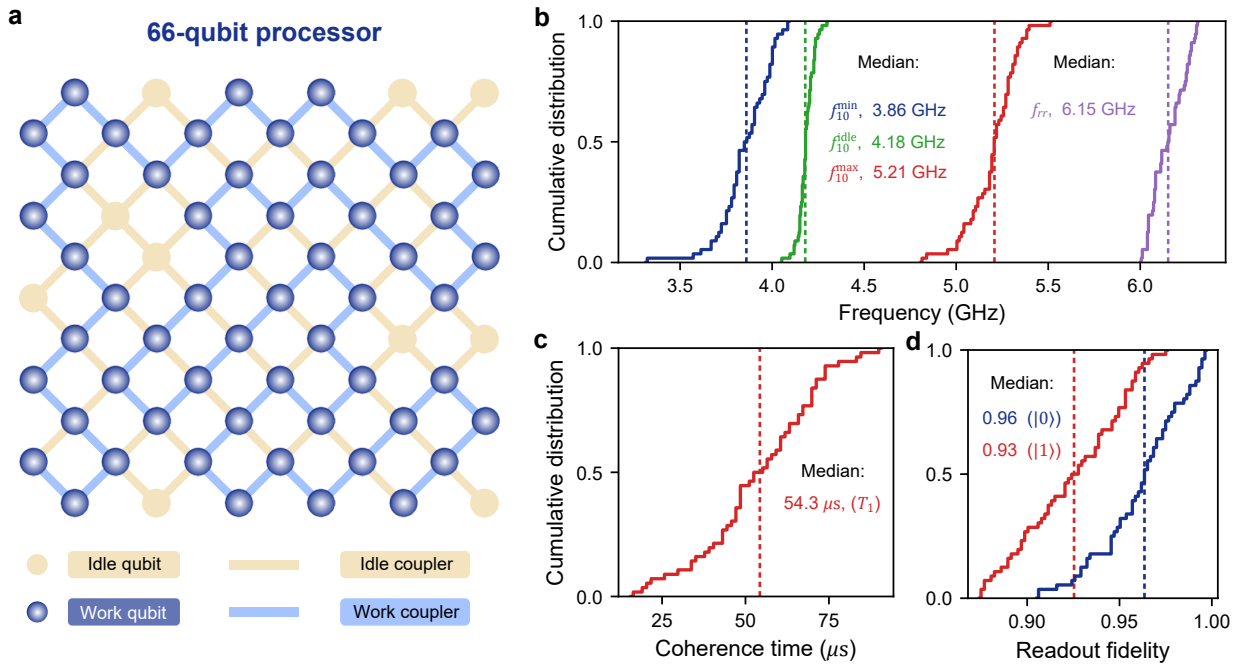

Supplementary Fig. S11. **Device performance.** **a** The layouts of qubits and couplers. **b** Cumulative distribution of the minimum frequency $f_{10}^{\min}$, maximum frequency $f_{10}^{\max}$, and idle frequency f_{10}^{idle} for the frequency-tunable qubit, and the frequency of readout resonator. **c** Cumulative distribution of qubit relaxation time T_1 measured at the idle frequency across the 56 qubits used in experiment. **d** Cumulative distribution of the qubit readout fidelities for $|0\rangle$ and $|1\rangle$ state.

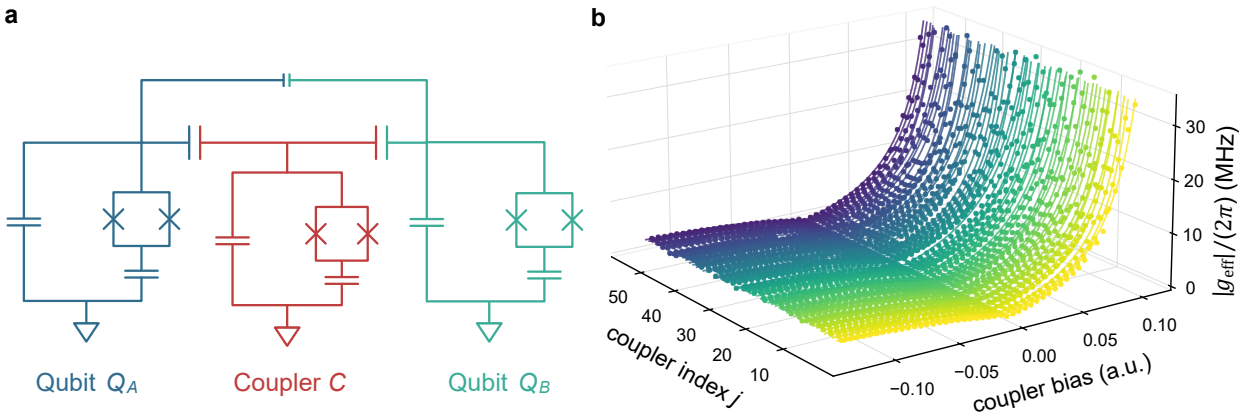

Supplementary Fig. S12. **Characterization of the tunable coupling.** **a** Circuit schematic for the qubit-coupler-qubit system. **b** The coupling strength $|g_{\text{eff}}|$ extracted from the vacuum Rabi oscillation between the neighboring qubits at different coupler bias.

coupler frequency is largely detuned from the qubits frequencies $|\omega_{A,B} - \omega_C| \gg g_{AC}, g_{BC}$,

the effective Hamiltonian of such a system is given as

$$H_{\text{eff}}/\hbar = \sum_{i=A,B} \left(\omega_i a_i^\dagger a_i + \frac{U_i}{2} a_i^\dagger a_i^\dagger a_i a_i \right) + g_{\text{eff}} \left(a_A^\dagger a_B + a_A a_B^\dagger \right), \tag{S53}$$

where the effective coupling strength

$$g_{\text{eff}} = g_{AB} + \frac{g_{AC} g_{BC}}{2} \left(\frac{1}{\omega_A - \omega_C} + \frac{1}{\omega_B - \omega_C} \right), \tag{S54}$$

can be modulated by tuning the coupler frequency ω_C through the flux bias line of the coupler. In experiments, we perform the vacuum Rabi oscillation between the first excited states of two qubits to characterize the effective coupling strength g_{eff} between qubits, where a Z control pulse is applied on the coupler with different coupler bias to change the strength of g_{eff}. Fig. S12b shows the characterization of the couplers $C_{j,j+1}$ connecting the qubits Q_j and Q_{j+1} in the 1D array, where the effective coupling strength g_{eff} can be continuously adjusted from +4 MHz to approximately −30 MHz [S16].

VI. ADDITIONAL EXPERIMENTAL RESULTS OF THE TIME EVOLUTION

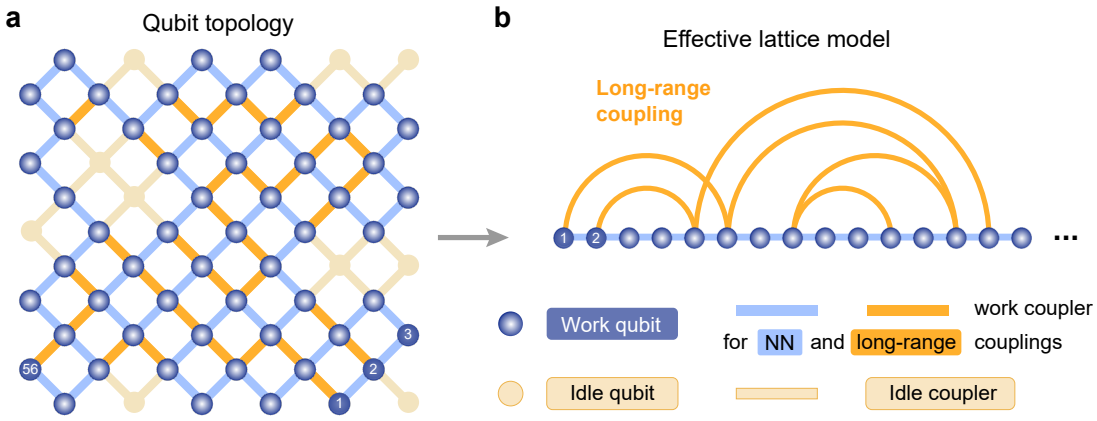

Supplementary Fig. S13. **1D quantum spin model with long-range coupling on a 2D array of spin qubits.** **a** The qubit topology for a 2D array of spin qubits. **b** The effective 1D quantum spin model with long-range coupling.

The 2D configuration enables us to emulate the processes with long-range coupling beyond the original 1D array with various controlled configurations, as shown in Fig. S13, which is used in Fig. 2e and f of the main text. In Fig. 2 of the main text, the dynamics of the critical

state in the mosaic lattice model shows uni-side quantum dynamics around the site $j = 14$ and $j = 47$. We further investigate the critical state dynamics in the presence of long-range couplings under different configurations of long-range couplings. We first show that the IDZs protected critical states are robust to the local perturbative long-range couplings, as long as the quasiperiodic modulation of hopping couplings and the overall IDZs persist. As

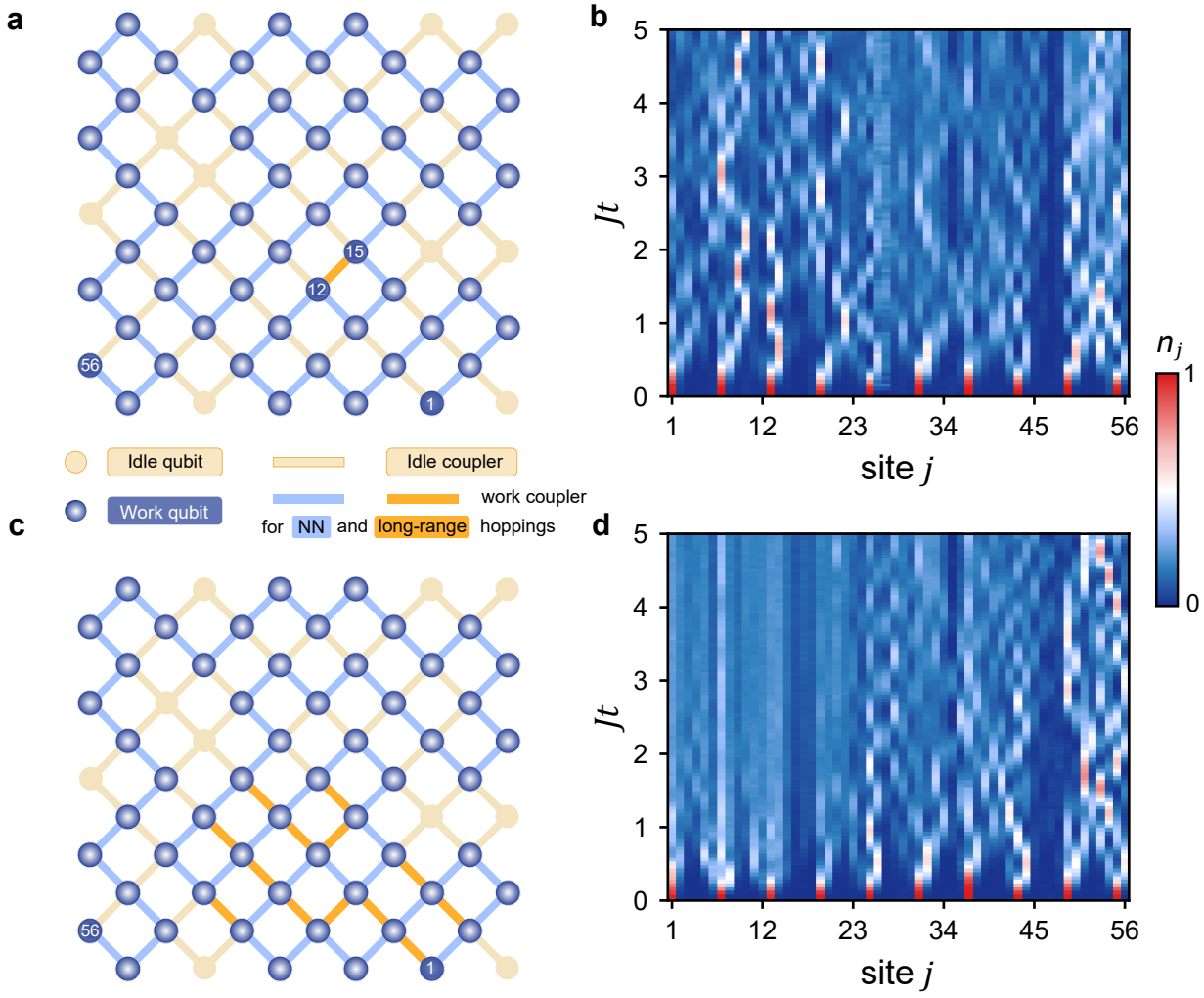

Supplementary Fig. S14. **Dynamics of the mosaic model in the presence of long-range coupling.** **a** Illustration for a 1D array with a single long-range coupling between the sites $12 \leftrightarrow 15$. **b** Measured dynamics in the configuration of a 1D array with long-range couplings as illustrated in **a**. **c** Illustration for a 1D array with more long-range couplings. **d** Measured dynamics in the configuration as illustrated in **b**. Here $\lambda/(2\pi) = 10$ MHz, $J/(2\pi) = 4$ MHz, $J^L_{m,n}/(2\pi) = 10$ MHz and $\phi = \pi/5$.

illustrated in Fig. S14a, when a single long-range coupling between the sites $12 \leftrightarrow 15$ is involved, only the largest zeros in the quasiperiodic hopping couplings are removed under this local perturbation. Fig. S14b shows the measured dynamics, and the density evolution pattern of critical states still persists. This indicates that the critical states are robust to the local perturbation of the IDZs.

Introducing more long-range couplings generically breaks the critical states. In Fig. S14c, we introduce the long-range coupling into half of the system, while keeping the IDZs in the rest of the system unchanged. Fig. S14d shows the characteristic dynamics of the extended state in the presence of long-range coupling. The unperturbed part, however, still shows non-ergodic dynamics.

[S1] S. Aubry and G. André, *Analyticity breaking and anderson localization in incommensurate lattices*, Ann. Israel Phys. Soc. **3**, 18 (1980).

[S2] A. Avila, *Global theory of one-frequency schrödinger operators*, Acta Mathematica **215**, 1 (2015).

[S3] A. Avila, S. Jitomirskaya, and C. A. Marx, *Spectral theory of extended Harper's model and a question by Erdős and Szekeres*, Invent. math. **210**, 283 (2017).

[S4] X.-C. Zhou, Y. Wang, T.-F. J. Poon, Q. Zhou, and X.-J. Liu, *Exact new mobility edges between critical and localized states*, Phys. Rev. Lett. **131**, 176401 (2023).

[S5] H. Li, Y.-Y. Wang, Y.-H. Shi, K. Huang, X. Song, G.-H. Liang, Z.-Y. Mei, B. Zhou, H. Zhang, J.-C. Zhang, S. Chen, S. P. Zhao, Y. Tian, Z.-Y. Yang, Z. Xiang, K. Xu, D. Zheng, and H. Fan, *Observation of critical phase transition in a generalized Aubry-André-Harper model with superconducting circuits*, npj Quantum Inf. **9**, 1 (2023).

[S6] X.-J. Liu, *Quantum matter in multifractal patterns*, Nat. Phys. **20**, 1851 (2024).

[S7] H. Hiramoto and S. Abe, *Dynamics of an Electron in Quasiperiodic Systems. II. Harper's Model*, J. Phys. Soc. Jpn. **57**, 1365 (1988).

[S8] J. Zhong, R. B. Diener, D. A. Steck, W. H. Oskay, M. G. Raizen, E. W. Plummer, Z. Zhang, and Q. Niu, *Shape of the Quantum Diffusion Front*, Phys. Rev. Lett. **86**, 2485 (2001).

[S9] Y. Wang, L. Zhang, S. Niu, D. Yu, and X.-J. Liu, *Realization and Detection of Nonergodic Critical Phases in an Optical Raman Lattice*, Phys. Rev. Lett. **125**, 073204 (2020).

[S10] K. J. Satzinger, Y. P. Zhong, H.-S. Chang, G. A. Peairs, A. Bienfait, M.-H. Chou, A. Y. Cleland, C. R. Conner, É. Dumur, J. Grebel, I. Gutierrez, B. H. November, R. G. Povey, S. J. Whiteley, D. D. Awschalom, D. I. Schuster, and A. N. Cleland, *Quantum control of surface acoustic-wave phonons*, Nature **563**, 661 (2018).

[S11] A. Dunsworth, A. Megrant, C. Quintana, Z. Chen, R. Barends, B. Burkett, B. Foxen, Y. Chen, B. Chiaro, A. Fowler, R. Graff, E. Jeffrey, J. Kelly, E. Lucero, J. Y. Mutus, M. Neeley, C. Neill, P. Roushan, D. Sank, A. Vainsencher, J. Wenner, T. C. White, and J. M. Martinis, *Characterization and reduction of capacitive loss induced by sub-micron josephson junction fabrication in superconducting qubits*, Appl. Phys. Lett. **111**, 022601 (2017).

[S12] S. Huang, B. Lienhard, G. Calusine, A. Vepsäläinen, J. Braumüller, D. K. Kim, A. J. Melville, B. M. Niedzielski, J. L. Yoder, B. Kannan, T. P. Orlando, S. Gustavsson, and W. D. Oliver, *Microwave package design for superconducting quantum processors*, PRX Quantum **2**, 020306 (2021).

[S13] S. Kosen, H.-X. Li, M. Rommel, R. Rehammar, M. Caputo, L. Grönberg, J. Fernández-Pendás, A. F. Kockum, J. Biznárová, L. Chen, C. Križan, A. Nylander, A. Osman, A. F. Roudsari, D. Shiri, G. Tancredi, J. Govenius, and J. Bylander, *Signal crosstalk in a flip-chip quantum processor*, PRX Quantum **5**, 030350 (2024).

[S14] E. A. Sete, A. Q. Chen, R. Manenti, S. Kulshreshtha, and S. Poletto, *Floating tunable coupler for scalable quantum computing architectures*, Phys. Rev. Appl. **15**, 064063 (2021).

[S15] X. Yang, J. Chu, Z. Guo, W. Huang, Y. Liang, J. Liu, J. Qiu, X. Sun, Z. Tao, J. Zhang, J. Zhang, L. Zhang, Y. Zhou, W. Guo, L. Hu, J. Jiang, Y. Liu, X. Linpeng, T. Chen, Y. Chen, J. Niu, S. Liu, Y. Zhong, and D. Yu, *Coupler-assisted leakage reduction for scalable quantum error correction with superconducting qubits*, Phys. Rev. Lett. **133**, 170601 (2024).

[S16] F. Yan, P. Krantz, Y. Sung, M. Kjaergaard, D. L. Campbell, T. P. Orlando, S. Gustavsson, and W. D. Oliver, *Tunable coupling scheme for implementing high-fidelity two-qubit gates*, Phys. Rev. Appl. **10**, 054062 (2018).

[S17] Y. Xu, J. Chu, J. Yuan, J. Qiu, Y. Zhou, L. Zhang, X. Tan, Y. Yu, S. Liu, J. Li, *et al.*, *High-fidelity, high-scalability two-qubit gate scheme for superconducting qubits*, Phys. Rev. Lett. **125**, 240503 (2020).